ARTICLE

Solar Cells Based on Junctions between Colloidal PbSe Nanocrystals and Thin ZnO Films

Kurtis S. Leschkies, Timothy J. Beatty, Moon Sung Kang, David J. Norris,* and Eray S. Aydil*

Department of Chemical Engineering & Materials Science, University of Minnesota, 421 Washington Avenue SE, Minneapolis, Minnesota 55455

ABSTRACT We report a new type of excitonic solar cell based on planar heterojunctions between PbSe semiconductor nanocrystals and thin ZnO films. These solar cells generate large photocurrents and higher photovoltages compared to Schottky cells assembled with similar nanocrystal films. When illuminated with 100 mW/cm^2 simulated AM1.5 spectrum, these solar cells exhibit short-circuit currents between 12 and 15 mA/cm^2, open-circuit voltages up to 0.45 V, and a power conversion efficiency of 1.6%. The photovoltage depends on the size of the nanocrystals, increasing linearly with their effective band gap energy.

KEYWORDS: nanocrystal · PbSe · ZnO · quantum dot · solar cell · excitonic solar cell

The unique optical and electronic properties of semiconductor nanocrystals (NCs) can be advantageous for solar cells.[1,2] In particular, due to the size-dependent quantization of their electronic levels, the optical transitions of NCs can be tuned to optimize absorption of the solar spectrum. The ability to control the energy levels with size also allows these levels to be positioned with respect to the band edge states of other semiconductors such that the direction of charge transfer can be tailored across heterojunctions formed between NCs and semiconductor films.[3] Moreover, semiconductor NCs can be prepared in large quantities as stable colloidal dispersions under mild conditions[4] and deposited as ordered or amorphous solids on surfaces of various geometries.[5] Consequently, a variety of solar-cell architectures that utilize semiconductor NCs have been developed and reported.[6−10]

In one scheme, commonly referred to as the bulk heterojunction solar cell, NCs are mixed with an organic semiconductor to form a continuous network of nanoparticles embedded in the organic phase.[11−15] Light is absorbed by both the NCs and the organic semiconductor to generate electron−hole pairs that are separated at the boundary between the NC and the organic semiconductor. The carriers are then transported in their respective phases and collected at opposing electrodes. In another scheme, nanoparticles or nanowires of wide band gap semiconductors, such as ZnO or TiO_2, are sensitized by II−VI[3,6,7,10,16−20] or III−V[21,22] semiconductor NCs. In these solar cells, electron−hole pairs are photogenerated in the NCs and electrons are transferred to the wide band gap semiconductor while the holes are either transferred to a hole conductor or reduced through an electrochemical reaction with a reductant in an electrolyte.

Alternatively, thin films of semiconductor NCs have recently been sandwiched between metal electrodes to form solar cells based on Schottky junctions without the need for separate electron and hole transport materials.[23−26] While these devices exhibit substantially higher photocurrents (>20 mA/cm^2 at short-circuit) compared to the NC-based solar cells described above, they produce relatively low voltages at open-circuit (~0.2 V), which limits their overall power conversion efficiency. The maximum open-circuit voltage (V_{oc}) in these devices has been shown to be limited to $E_g/2e$, where E_g is the effective band gap energy of the NC and e is the electron charge.[24] Therefore, no NC approach has demonstrated both high photocurrents and high V_{oc}.

Here, we address this problem by replacing the Schottky junction with a heterojunction formed between a thin film of NCs and a semiconductor. Specifically, we utilize colloidal PbSe NCs and a thin film of ZnO. We show that such devices provide a new kind of solar cell that can produce open-circuit voltages as high as ~0.45 V. Our solar cells resemble traditional photo-

*Address correspondence to aydil@umn.edu, dnorris@umn.edu.

Received for review July 3, 2009 and accepted October 12, 2009.

Published online October 20, 2009. 10.1021/nn901139d CCC: $40.75

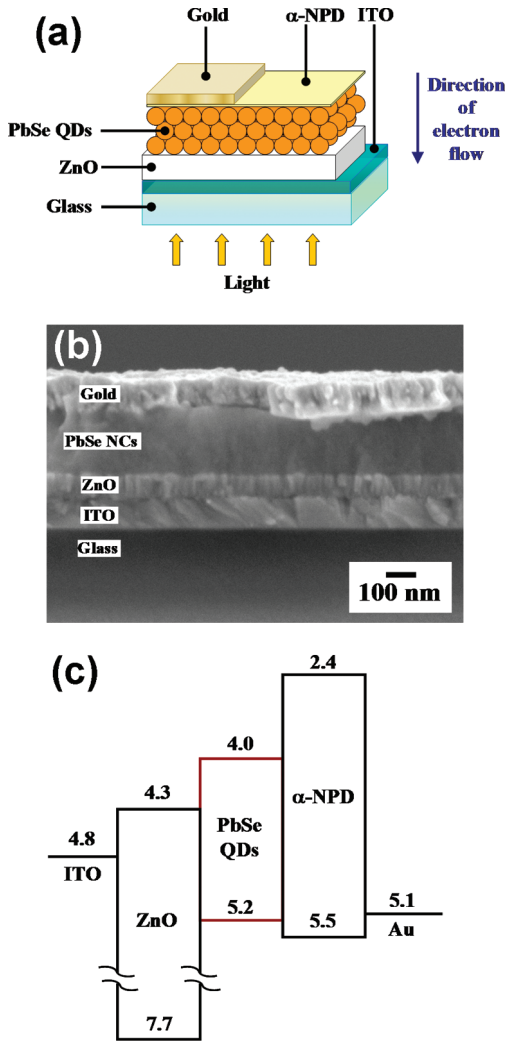

Figure 1. (a) Schematic of the PbSe NC/ZnO heterojunction solar cell. (b) Cross-sectional scanning electron micrograph (SEM) of the PbSe NC/ZnO junction solar cell illustrated in (a). A 15 nm thick α-NPD layer, while present, could not be resolved with SEM. (c) Schematic of an energy band diagram of an ITO/ZnO/PbSe NC/α-NPD/gold stack 1.5. Energetic positions of all semiconductor band edges and metal work functions are reported with respect to vacuum and have units of eV. The position of the electron and hole level for PbSe is representative of ~2.5 nm NCs and calculated using the band gap energy and electron affinity of bulk PbSe and assuming equal shift in the position of the electron and hole levels as a consequence of size quantization. The position of the band edges of α-NPD was taken from ref 30. The schematic is drawn such that interfacial effects on all semiconductor band edges and metal work functions are neglected when the device materials are put into contact.

voltaic devices based on a semiconductor−semiconductor heterojunction but with the important difference that the band gap of one of the semiconductors, and consequently the cell's photovoltage, can be varied by changing the size of the NCs.

RESULTS AND DISCUSSION

Our device, depicted in Figure 1a,b, is fabricated by depositing thin films (80−100 nm) of ZnO and PbSe NCs onto an indium−tin−oxide (ITO)-patterned glass substrate. The transparent and conducting ITO layer has a resistance of 8−12 Ω/□ and forms the bottom contact of the device. A 100 nm thick gold film is used as the top contact and is deposited by evaporation either directly onto the PbSe NC film or onto a thin (15−30 nm) α-NPD [*N*,*N*′-bis(1-naphthalenyl)-*N*,*N*′-bis(phenylbenzidine)] layer.

In all solar cells discussed below, ZnO films were deposited at room temperature directly onto ITO-coated glass substrates from a ZnO target using radio frequency reactive magnetron sputtering with Ar and O_2 gases. Prior to deposition, the ITO layer was patterned to produce bottom electrodes for six separate solar cells on a single substrate. The ZnO films are oriented along the [0001] direction; X-ray diffraction of the sputtered ZnO films (Figure S1 in Supporting Information) showed a single diffraction peak at $2\theta = 34.4°$, which corresponds to the (0002) lattice plane of ZnO. Scherrer analysis of this diffraction peak indicates that the film consists of oriented grains that are 30−40 nm in size.

Separately, we synthesized PbSe nanocrystals directly from PbO according to ref 27 and 28. When colloidal PbSe NCs are cast onto ZnO, the resulting glassy films are electrically insulating with a conductance on the order of 10^{-10} S/cm in the dark. This is consistent with previous reports[5] and is due primarily to the bulky nature of the ligands on the NC surface (*e.g.*, oleic acid and tri-*n*-octylphosphine) that inhibit charge transport. These bulky ligands must be removed completely or replaced with shorter ligands to increase electronic coupling between the NCs.[5,29] To accomplish this, we used a layer-by-layer technique[23,24] wherein the substrate is alternately dipped into a colloidal dispersion of PbSe NCs and a solution containing a short ligand (*e.g.*, hydrazine or 1,2-ethanedithiol, EDT). This two-step dip-coating process was repeated until the desired thickness was achieved. The thickness per step depends on the NC concentration in the colloidal dispersion and the removal speed. Rotating the substrate 90° between successive coatings improves the macroscopic uniformity of deposition. We found that our solar cells were most efficient when the PbSe NC films were 150−200 nm thick. The NC films deposited were crack-free and exhibited electrical conductance values of 10^{-5}−10^{-4} S/cm in the dark, as in ref 28. Field-effect transistors (FETs) made with these EDT-treated films demonstrate ambipolar gating (Figure S2 in Supporting Information), but with asymmetric transfer characteristics in which the electron current and mobility are higher than the hole current and mobility. This asymmetry was observed both in the dark and under 10.5 mW/cm^2 broad-band illumination. We note that using hydrazine to wash the NC films resulted in little or no deposition of NCs onto the ZnO. For this reason, we did not use hydrazine to treat the NCs while using the layer-by-layer dip-coating method to deposit films.

In the solar cells depicted in Figure 1, light is absorbed by the NCs, producing photoexcited electron−hole pairs that are confined within the NCs. These electron−hole pairs may (i) recombine, (ii) dissociate, either at a NC−electrode interface or within the NC film, particularly if a strong electric field exists, or (iii) move across the NC film as excitons. If the electron−hole pair dissociates prior to encountering an electrode, the separated electrons and holes can either diffuse or drift under the influence of the electric field toward opposite collection electrodes and generate a photocurrent. If the electron−hole pair dissociates at the NC−ZnO interface, electrons can lower their energy by transferring into the ZnO film, which forms a type-II heterojunction with the PbSe NCs (Figure 1c). These electrons move across the ZnO film and are collected at the ITO contact. The positive charges left behind in the NC film are transported to and collected at the gold electrode.

It is also possible for electron−hole pairs to dissociate at the NC−gold interface. When this occurs, the hole should be transferred from the PbSe NCs to the gold for proper solar-cell operation; hole transfer in this direction would produce photocurrent in the opposite direction of the forward bias dark current and generate power. However, electrons can also transfer to the gold contact since this process is also energetically favorable; this electron transfer would produce a shunt current that opposes the photocurrent and limit the solar-cell efficiency. We sought to block this parasitic flow of electrons by inserting a thin layer of α-NPD between the PbSe NCs and gold film. α-NPD is commonly used in organic light-emitting devices[31,32] and solar cells[33] as a hole injection and hole transport layer. Moreover, α-NPD protects the NCs from physical damage during metal evaporation. When an α-NPD layer is present between the PbSe NCs and gold film, the electrons would have to increase their energy markedly in order to transfer to the gold contact from the PbSe NCs (Figure 1c). Consequently, α-NPD was used in our solar cells to block the transfer of electrons at the PbSe−gold interface.

Figure 2 shows the *I*−*V* characteristics of our best solar cell, which was assembled using a 200 nm thick EDT-treated PbSe NC film made from ~3 nm diameter NCs deposited onto a ZnO film annealed at 450 °C with 15 nm thick α-NPD layer inserted between the PbSe NCs and the gold contact. This solar cell exhibited a short-circuit current density, J_{sc}, of 15.7 mA/cm^2, V_{oc} of 0.39 V, and an overall power conversion efficiency of 1.6% when illuminated with 100 mW/cm^2 simulated AM1.5 light. The direction of the photocurrent in forward bias was consistent with electrons flowing from the gold metal contact to the PbSe NC film and into the ZnO. This direction is opposite to that observed in the Schottky solar cells described in refs 23 and 24, where the excitons dissociate in the space charge layer near the interface between the top metal contact and NC film and the separated electrons flow from the NCs to the metal contact. Moreover, the V_{oc} of 0.39 V is substantially larger than that observed in Schottky solar cells that use a gold top contact (~0.06 ± 0.03 V). Both of these differences indicate that the mechanism of photocurrent generation in our heterojunction solar cells is different than that in the Schottky solar cells described in refs 23 and 24.

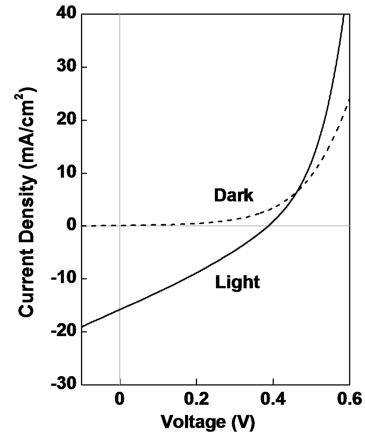

Figure 2. Current−voltage (*I*−*V*) characteristics of a PbSe NC/ZnO heterojunction solar cell recorded in the dark and under 100 mW/cm^2 simulated AM1.5 illumination. The solar cell was assembled using (i) ~200 nm thick EDT-treated PbSe NC film deposited from ~2.8 nm diameter NCs, (ii) 80−100 nm thick ZnO film annealed at 450 °C, and (iii) 15 nm thick α-NPD layer between the PbSe and gold contact. Fill factor, V_{oc}, J_{sc}, and overall power conversion efficiency of this cell were 0.27, 0.39 V, 15.7 mA/cm^2, and 1.6%, respectively.

Figure 3 displays the wavelength dependence of the incident-photon-to-current-conversion efficiency (IPCE, or external quantum efficiency) for the solar cell shown in Figure 2. This PbSe NC-based solar cell generates photocurrent that spans the spectral region from the near-infrared (1200 nm) into the visible (400 nm). The shape of the photoaction and IPCE spectra closely resemble the optical absorption spectrum of the PbSe NCs from 400 to 1200 nm. In fact, the spectrally resolved

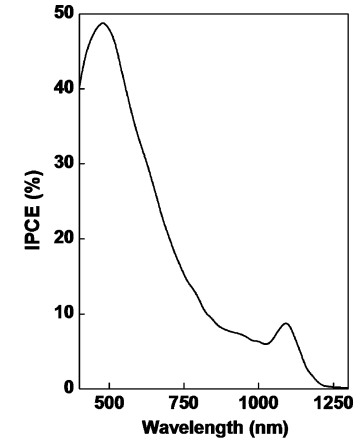

Figure 3. Incident photon-to-current conversion efficiency (IPCE) spectrum of the NC solar cell featured in Figure 2. The position of the first excited state in the PbSe NC film is at 1104 nm.

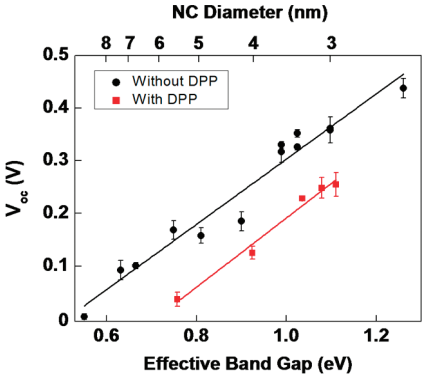

Figure 4. Dependence of V_{oc} on the diameter and effective band gap energy (E_g) for NCs synthesized with and without DPP. All solar cells were assembled using ~250 nm thick EDT-treated PbSe NC film deposited onto 80−100 nm thick ZnO with a 20 nm thick α-NPD layer. Each data point corresponds to an average of six solar cells fabricated on the same substrate. The error bars for each point represent one standard deviation of these six devices. Solid lines are least-squares linear fit to the data points.

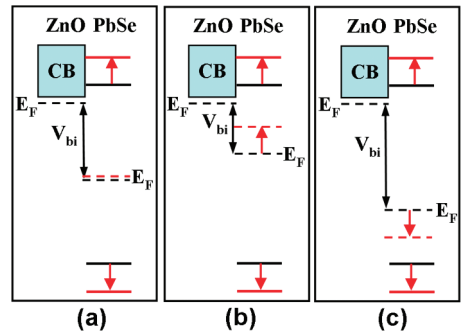

Figure 5. Energy band diagrams for ZnO/PbSe NC heterojunctions where the PbSe NC films are (a) intrinsic, (b) doped n-type, and (c) doped p-type. Arrows indicate the directions in which energy levels would move as the size of the NC is decreased. In (a), regardless of NC size, E_F in PbSe does not shift with respect to the Fermi level in ZnO. In (b), decreasing NC size shifts E_F in PbSe closer to E_F in ZnO and the built-in potential, V_{bi}, should decrease as a result of this shift. In (c), decreasing NC size shifts E_F in PbSe away from E_F in ZnO, thus increasing the built-in potential. Valence band of ZnO is below all levels shown in this diagram and omitted for clarity. Band bending is not shown.

peak at 1100 nm in the IPCE aligns precisely with the position of the first excited state in the PbSe NC film (1104 nm). Thus, we conclude that the photocurrent generated between 400 and 1200 nm is due to the photogeneration of electron−hole pairs within the PbSe NCs followed by electron transfer to ZnO.

The photovoltage of our solar cells could be tuned by changing NC size and hence the electronic energy levels within the NCs. For example, Figure 4 shows the variation of V_{oc} for solar cells assembled using different size NCs as a function of the effective NC band gap, E_g. We collected this data for solar cells whose PbSe NCs were synthesized with and without diphenylphosphine (DPP). In both cases, V_{oc} increases linearly with increasing E_g (or decreasing NC size and increasing quantum confinement). A linear fit to the data for NCs that were synthesized without DPP yields $V_{oc} = 0.60(E_g/e) - 0.31$, where E_g and V_{oc} have units of eV and V, respectively. Clearly, the location of the electronic energy levels in the NCs determines the amount of V_{oc} in our solar cells; quantum confinement is maintained within the individual NCs even though they are electronically coupled to each other to provide charge transport throughout the NC film. Furthermore, this result suggests that quantum confinement within NCs is necessary to obtain functional solar cells since using bulk PbSe ($E_g = 0.27$ eV) would not generate photovoltage. The highest V_{oc} we obtained was 0.45 V with ~2.3 nm diameter PbSe NCs.

One possibility which describes the operating principle in our solar cells is that the PbSe NC−ZnO junction is behaving like a traditional heterojunction diode solar cell between two dissimilar semiconductors and that V_{oc} is determined by a built-in junction potential, V_{bi}, the difference in the location of the Fermi levels between the ZnO and PbSe NC film.[34] However, this possibility is difficult to reconcile with the observed increase in V_{oc} with NC size (Figure 4). In undoped EDT-treated NC films, the Fermi level should be positioned midway between the lowest electron and hole energy levels and remain fixed regardless of NC size (Figure 5a). Since the Fermi level in the ZnO is close to the conduction band and independent of PbSe NC size, V_{bi} and hence V_{oc} should not change with NC size. This is contrary to the experimental observation in Figure 4. For an n-type PbSe NC film, as Figure 5b illustrates, an increase in the effective band gap of the NCs would shift the NC Fermi level up and closer to the Fermi level in ZnO. This in turn would cause V_{oc} to decrease with increasing E_g (or decreasing NC size), opposite to the trend displayed in Figure 4. An increase in V_{oc} with NC size is possible for a p-type PbSe NC film since the NC Fermi level would shift down with respect to the Fermi level location in ZnO, as depicted in Figure 5c. However, FET transfer characteristics show that our EDT-treated PbSe NC films are not p-type but exhibit ambipolar conduction with higher electron current both in the dark and under illumination. While we cannot completely eliminate the possibility that the PbSe NC films in solar cells become p-type for some reason, we conclude that our solar cells are unlikely to be operating like traditional p−n heterojunction solar cells.

A second possibility is that our solar cells operate like excitonic solar cells,[35] formed by adjoining donor and acceptor materials wherein excitons created by light absorption are dissociated at the donor−acceptor junction to create photocurrent. In excitonic solar cells, the V_{oc} depends on, and increases with, the difference between the lowest unoccupied molecular orbital (LUMO) level of the acceptor and the highest occupied molecular orbital (HOMO) level of the donor. In our solar cells, the LUMO and HOMO levels would correspond, respectively, to the conduction band edge of the ZnO and the lowest energy level for holes in the NC film. This

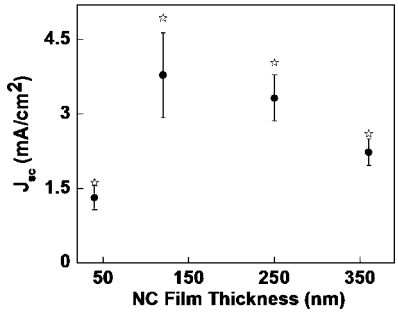

Figure 6. Dependence of J_{sc} on PbSe NC film thickness for solar cells assembled using ~4 nm diameter PbSe NCs. Error bars are determined as in Figure 4. The star symbol corresponds to the best result from the set of six solar cells.

difference depends on and increases with decreasing NC size and would explain the observed trend in Figure 4. Moreover, the photocurrent is reduced to zero for PbSe NC sizes that place the lowest electron energy level in the NC below the ZnO conduction band edge. This observation suggests that photogenerated electron−hole pairs in the PbSe NCs dissociate at the PbSe−ZnO interface and the photovoltaic effect is lost when the driving force for electron−hole dissociation *via* electron transfer to ZnO vanishes. However, we note that, regardless of the mechanism of operation of our solar cells, they constitute a novel class of semiconductor film/NC film heterojunction solar cells wherein the photovoltage depends on the NC size and the extent of quantum confinement within the NCs.

We also observe that the variation of V_{oc} with E_g is strongly affected by the addition of DPP during NC synthesis. For solar cells assembled from PbSe NCs prepared with DPP, a linear fit to the data in Figure 4 yields $V_{oc} = 0.62(E_g/e) - 0.46$ V. Thus, omitting DPP during NC synthesis results in an increase of approximately 0.15 V in V_{oc} for all NC sizes.

We also studied the effects of (i) PbSe NC film thickness, (ii) α-NPD blocking layer thickness, and (iii) the properties of the ZnO film on solar-cell performance. Figure 6 shows the dependence of J_{sc} on PbSe NC film thickness for solar cells assembled using ~4 nm diameter NCs. Initially, the photocurrent increases with NC film thickness because additional electron−hole pairs created in thicker films can be dissociated, separated, and extracted from the device. However, J_{sc} peaks when the film thickness is ~100 nm and does not increase for thicker films. This trend was also reported in Schottky solar cells made from similar PbSe NC films[36] and is expected if the diffusion length of excitons or charge carriers in the PbSe NC films is ~100 nm. Within our experimental error, V_{oc} and the fill factor did not change with increasing PbSe NC film thickness.

The α-NPD blocking layer prevents the flow of photogenerated electrons from the PbSe NCs to the gold electrode and increases the shunt resistance in our solar cells. We estimated the shunt resistance of the solar cells assembled with and without the α-NPD blocking

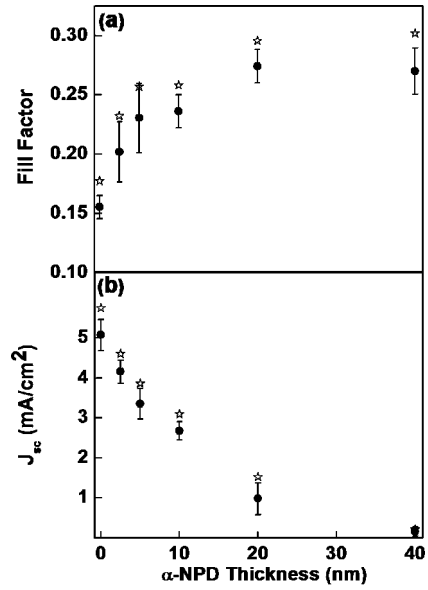

Figure 7. Dependence of (a) fill factor and (b) J_{sc} on α-NPD thickness for solar cells assembled using ~280 nm thick EDT-treated PbSe NC film deposited onto 80−100 nm thick ZnO from ~4.3 nm diameter NCs. Error bars are determined as in Figure 4. The star symbol corresponds to the best result from the set of six solar cells.

layer by fitting their $I-V$ characteristics measured under illumination to an equivalent circuit model (Supporting Information).[37] We found that when a 30 nm thick α-NPD film is inserted between the NCs and the gold electrode the shunt resistance increases by an order of magnitude, from ~9−20 to ~100−200 Ω (Figures S3 and S4 in Supporting Information). This thin α-NPD blocking layer also improves the fill factor of the solar cells and eliminates negative curvature in the $I-V$ characteristics (see Figure S3), commonly referred to as "double diode" behavior.[38] Figure 7a shows this improvement in fill factor with increasing thickness of the α-NPD blocking layer. This observation is consistent with the hypothesis that α-NPD reduces the dissociation of electron−hole pairs at the gold contact and blocks the transfer of electrons from PbSe to gold during illumination. Saturation of the fill factor with α-NPD thickness suggests that a minimum thickness of about ~30 nm is needed to block the shunt current.

While electron flow from the PbSe NCs to the gold electrode must be eliminated, the holes arriving at the gold electrode through the PbSe NC film must still be able to recombine with electrons in the gold to provide continuous current flow. Several mechanisms are possible for electron−hole recombination at the NC−α-NPD and α-NPD−gold interfaces or within the α-NPD layer. For example, when the α-NPD layer is very thin, it is possible for holes to tunnel from the PbSe NCs to the gold through the blocking layer. Tunneling or hopping of holes from the NCs directly into the α-NPD layer is also possible. Once in α-NPD, the holes can be transported by hopping from trap-to-trap or between α-NPD molecules to the gold electrode. Alternatively, electron

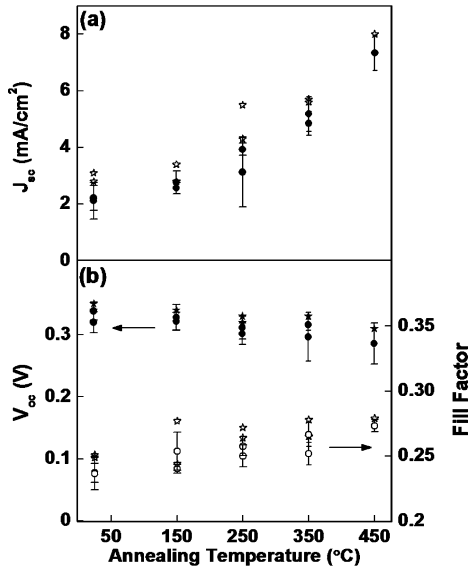

Figure 8. Dependence of (a) J_{sc}, (b) V_{oc}, and fill factor as a function of ZnO film annealing temperature for devices assembled using ~250 nm thick EDT-treated PbSe NC film deposited from ~3.2 nm diameter NCs with an 18 nm thick α-NPD layer. Data points at 25 °C refer to an as-deposited (not annealed) ZnO film. Error bars are determined as in Figure 4.

tunneling or hopping in the reverse direction from gold into α-NPD could occur. In this case, electrons can neutralize the holes within the α-NPD layer; however, α-NPD generally exhibits poor electron mobility and transport and is presumed to be a hole-only material.[32] While the dominant mechanism of current flow across the NC−α-NPD and α-NPD−gold interfaces or within the α-NPD layer is not known, in all of the potential mechanisms, the probability of electron−hole recombination decreases with increasing α-NPD layer thickness, effectively blocking the current flow. Indeed, Figure 7b shows that J_{sc} decreases exponentially with α-NPD thickness. Electronic doping has been shown to improve hole injection and transport in thick α-NPD films and remains a possible future direction for improving the solar-cell efficiency.[39,40]

The processing conditions and properties of the ZnO film also affect the performance of our solar cells. Specifically, reducing the O_2 flow rate during sputtering and annealing the ZnO film after deposition both lead to solar cells with higher photocurrents, fill factor, and power conversion efficiencies. For example, Figure 8a,b shows measured values of J_{sc}, V_{oc}, and fill factor for solar cells assembled using ZnO films that were sputtered using Ar gas and then subsequently annealed in air at temperatures up to 450 °C. We found that J_{sc} increases significantly from ~2 to 7 mA/cm^2 while the fill factor increases from ~0.24 to 0.27 as a function of the annealing temperature; open-circuit voltage decreases only slightly as the annealing temperature is increased from 150 to 450 °C.

We attribute these changes in part to improvements in ZnO electrical conductance (σ) and electron mobility. This conclusion is based on the electrical characteristics of FETs made using ZnO films that are deposited under the same conditions. We found that the electrical conductance in the dark (σ_{dark}) of the n-type ZnO films increased over an order of magnitude as O_2 flow in the sputtering gas was reduced from 3 sccm O_2 to 0 (sputtering with Ar gas only). The conductance, field-effect electron mobility ($\mu_{e,sat}$, obtained in the saturation regime of the transfer curve), and electron density (n, calculated from $\sigma_{dark} = ne\mu_{e,sat}$) are listed in Table 1 for different sputtering conditions (see also Supporting Information). Since the electron density in our ZnO films decreases as the amount of oxygen used during deposition is reduced, the measured increase in conductance is entirely due to the increase in the electron mobility in ZnO with decreasing O_2 flow rate.

TABLE 1. Electrical Conductance (σ_{dark}), Electron Field-Effect Mobility ($\mu_{e,sat}$), and Electron Density (n) (averaged over three devices) of ZnO Deposited at Room Temperature from Various Combinations of Sputtering Gases

sputtering gas	σ dark (S/cm)	$\mu_{e,sat}$ (cm^2/V/s)	n (cm^{-3})
15 sccm Ar/5 sccm O_2[a]			
17 sccm Ar/3 sccm O_2	9.3×10^{-8}	1.0×10^{-5}	5.7×10^{16}
19 sccm Ar/1 sccm O_2	4.9×10^{-7}	6.3×10^{-5}	3.9×10^{16}
20 sccm Ar	1.1×10^{-6}	4.8×10^{-4}	1.4×10^{16}

[a]Conductance and mobility could not be calculated because current levels could not be distinguished from noise.

The electrical conductance and electron mobility in ZnO also increase with increasing annealing temperature. Figure 9 shows the dependence of σ_{dark}, $\mu_{e,sat}$, and n on annealing temperatures ranging from 150 to 450 °C. In these experiments, ZnO films were sputtered using Ar gas only. We found that $\mu_{e,sat}$ improves by nearly two orders of magnitude when the ZnO is annealed at 150 °C in air compared to the as-deposited film (data point at 25 °C). As the annealing temperature is further increased, $\mu_{e,sat}$ increases by an additional order of magnitude over a temperature range of 150−450 °C. As a result, the electrical conductance of ZnO in the dark steadily increases from 10^{-6} S/cm for the as-deposited film to ~3×10^{-5} S/cm for a film annealed at 450 °C.

Annealing the ZnO films improves the electrical characteristics of ZnO and, hence, the performance of our solar cells in the following ways. First, it has been hypothesized that native point defects, such as zinc and oxygen vacancies or interstitials, are responsible for the unintentional n-type electrical conduction commonly observed in ZnO; however, the individual role of each defect is still being debated.[41,42] Recently, the incorporation of extrinsic hydrogen has also been proposed as a possible cause for the n-type conductance in ZnO.[43,44] Regardless of the specific mechanism and defect type, the defects, which donate charge and act as scattering centers, can be annealed as the temperature of

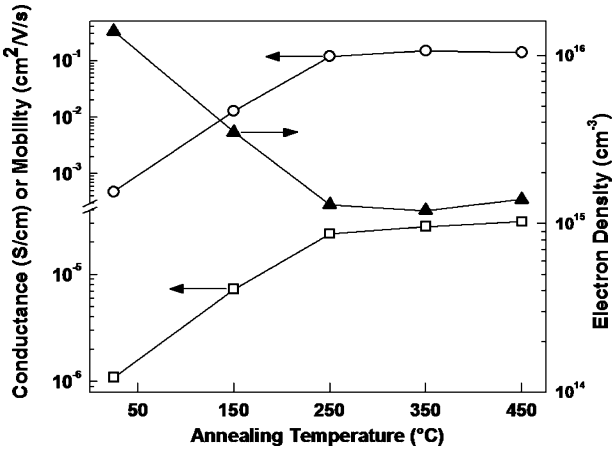

Figure 9. Dependence of ZnO film conductance (□), mobility (○), and electron density (▲) on post-sputtering annealing temperature. Each data point is averaged over three separate devices. The data point at 25 °C is for an as-deposited (not annealed) ZnO film. Lines connecting each data point represent a guide for the eye.

the ZnO film is increased. Consequently, by reducing the number of scattering centers in the ZnO film, the conductance and field-effect mobility of electrons are improved with increasing annealing temperature. The decrease in the electron density with increasing annealing temperature is consistent with both annealing of oxygen vacancies and/or desorption of H from the film. Residual water vapor in the sputtering chamber makes H ubiquitous. As a result, H can easily incorporate into ZnO as OH during sputtering and dope it n-type. Annealing can reduce H in ZnO films and reduce the electron density. Second, Scherrer analysis of the X-ray diffraction peaks from ZnO films annealed at different temperatures suggests that ZnO crystals grow during annealing. During this process, one- and two-dimensional defects, such as dislocations and grain boundaries, are also removed. Eliminating such defects decreases grain boundary electron scattering and increases the electron mobility and conductance in the ZnO film.

Finally, we note that, for each device that we assembled, the $I-V$ characteristics in the dark and under illumination intersect each other under forward bias. This "crossover" phenomenon has been reported in various thin film solar cells based on cadmium chalcogenides and Cu(In,Ga)Se_2 (CIGS).[45−51] While the exact reason for the crossover occurrence in our solar cells is unclear, several mechanisms have been proposed to explain this phenomenon in other thin film solar cells that may be applicable in our case.[44,48] For example, it has been suggested that the density of photogenerated carriers at or near the junction(s) between the active layers of the solar cells causes the electrical potential to be redistributed during illumination. This is possible particularly if one or more of the active layers in the solar cells is intrinsic and can be easily compensated by the presence of photogenerated carriers. The change in the electrical field may lead to the reduction of a light-modulated barrier located at various junctions when the solar cell is in forward bias. Regardless of the mechanism, the superposition principle for current is no longer valid in our solar cells and leads to crossover between the dark and light $I-V$ characteristics. Such changes under illumination may also be responsible for the low fill factor. Comparison of the $I-V$ characteristics in the dark and under illumination (Figure 2) shows that the shunt resistance is much higher in the dark but is reduced significantly when the cell is illuminated. This decrease in shunt resistance is one of the reasons for the low fill factor. Appearance of a similar photoshunt and low fill factors has also been observed in dye-sensitized solar cells made from ZnO[52−55] and may be associated with the ZnO film. Using another acceptor such as a thin layer of TiO_2 may improve the fill factor.

CONCLUSIONS

We have assembled solar cells based on heterojunctions between PbSe NCs and thin film ZnO that feature large photocurrents and higher V_{oc} values compared to Schottky solar cells with similar NC films. Optimizing the processing conditions of the thin film ZnO and α-NPD layer produces solar cells with typical J_{sc} values of 12−15 mA/cm^2, V_{oc} values up to 0.45 V, and overall power conversion efficiencies as high as 1.6%. Still, the performance of solar cells with this particular architecture can potentially be enhanced further with the following strategies. While it appears that an electron blocker is required between the NCs and top contact, α-NPD may not be the best possible candidate because of the location of its HOMO level. Materials whose HOMO level is better matched with the lowest hole energy level in the NCs may help improve hole transport across this junction. Another strategy to improve the efficiency of these solar cells is to use vertically oriented nanostructures, such as ZnO nanowires, instead of planar films. The nanowires would create additional interfacial area for exciton dissociation compared to planar films. Moreover, the distance between neighboring nanowires can be reduced to less than the exciton or carrier diffusion length in the PbSe NC film, thereby increasing the exciton or carrier collection efficiency. The prototypical devices presented herein form a promising starting point for such improvements.

METHODS

Chemicals and Substrates. Selenium shot (Se, 99.999%), aluminum shot (Al, 99.999%), and chromium pellets (Cr, 99.2%) were purchased from Alfa Aesar. *N*,*N*′-Bis(naphthalene-1-yl)-*N*,*N*′-bis(phenyl)benzidine (α-NPD) was purchased from Rubipy Scientific, Inc. Acetone (ACS grade) and isopropyl alcohol (IPA, ACS grade) were purchased from Mallinckrodt Chemicals. Anhydrous 200 proof ethanol (≥99.5%), anhydrous methanol (99.8%), anhy-

drous butanol (99.8%), anhydrous octane (≥99%), anhydrous hexane (≥99%), anhydrous acetonitrile (99.8%), 1,2-ethanedithiol (EDT, ≥98%), tri-*n*-octylphosphine (TOP, technical grade, 90%), oleic acid (technical grade, 90%), 1-octadecene (90%), lead(II) oxide (PbO, 99.999%), and diphenylphosphine (DPP) were purchased from Aldrich. All chemicals were used as delivered except for anhydrous hexane, which was dried over activated alumina prior to use. Polished indium−tin−oxide (ITO)-coated glass substrates (8−12 Ω/□) were purchased from Delta Technologies, Ltd. Then, ⟨100⟩-oriented, boron-doped silicon (Si) wafers (ρ = 0.005−0.01 Ω·cm, thickness = 525 ± 25 μm) coated with 300 nm of thermal oxide (SiO_2) growth were purchased from Silicon Valley Microelectronics. Gold shot (Au, 24-karat) used for photocathodes was purchased from W. E. Mowry.

Patterning of ITO-Coated Glass Substrates. ITO-coated glass substrates were patterned using optical lithography. Unpatterned, polished ITO-coated glass substrates were first cleaned by ultrasonication in an equal volume mixture of acetone, IPA, methanol, and deionized (DI) water for 60 min prior to patterning. Once cleaned, the substrates were dehydrated for 2 min at 115 °C and then exposed to hexamethyldisilazane (HMDS) vapor for 3 min to promote adhesion for the photoresist. MICROPOSIT S1818 positive photoresist was spin-coated onto the ITO-coated glass substrates at 3000 rpm for 60 s, and the residual solvent was driven from the photoresist by baking the substrates at 105 °C for 5 min prior to exposure. The photoresist-coated substrates were then exposed to UV radiation (Oriel model 8095 flood exposure system) with a predefined pattern using a chrome mask for 20 s. The exposed photoresist was developed by immersing the exposed substrates into a solution of MICROPOSIT MF-319 developer for 75 s and then immediately rinsed with deionized (DI) water and dried with nitrogen gas. The unexposed photoresist was hardened by baking at 120 °C for 20 min. The photoresist pattern masked the underlying ITO during etch. ITO was removed from unmasked regions of the surface by immersing the substrates into a heated (50 °C) mixture of 5% nitric acid and 20% hydrochloric acid (by volume in water) for 3 min, followed by a DI water rinse. Finally, the unexposed photoresist was removed from the substrates in a gently agitated acetone bath, leaving behind the desired ITO pattern. Each ITO-patterned glass substrate allowed for construction of up to six functional solar cells.

Deposition of Thin Film ZnO. Thin film ZnO was deposited through a shadow mask onto ITO-patterned glass substrates from a ZnO target (Williams Advanced Materials) using a radio frequency (RF) magnetron sputtering system (ATC 2000, AJA International). Prior to introducing the sputtering gas, the deposition chamber was evacuated to a pressure less than 10^{-6} Torr. The ionized sputtering gas used during deposition was a mixture of argon (Ar) and oxygen (O_2), supplied at various flow rates depending on the experiment. Effect of the gas flow rates was examined by varying the flow rates of Ar and O_2 gas from 20 sccm Ar with no O_2 flow to 15 sccm Ar with 5 sccm O_2. The initial process pressure inside the deposition chamber required to strike the plasma was set to 20 mTorr but reduced to 5 mTorr during sputtering of ZnO. The ZnO was deposited at room temperature onto the patterned ITO at a rate of 0.55 Å/s when operating the sputtering system at 200 W of RF power. Sputtered ZnO films were typically 80−100 nm thick.

Synthesis of Colloidal PbSe Nanocrystals. PbSe nanocrystals were synthesized based on methods developed by Murphy *et al.*[27] and Luther *et al.*[28] In a typical synthesis, PbO (5.0 g), oleic acid (18.1 mL), and 1-octadecene (70.3 mL) were placed in a four-neck round-bottom flask and heated to 40 °C. The reaction flask was then degassed to <10 mTorr while stirring vigorously and purged with dry nitrogen gas to remove atmospheric gases from inside of the flask. This degassing process was repeated three times. The reaction vessel was heated to 165 °C under nitrogen and was maintained at that temperature for approximately 40 min while the precursor solution turned optically clear. The precursor solution temperature was then lowered to 145 °C. Meanwhile, a solution of Se in TOP (1.0 M, 42 mL total volume) was prepared and loaded into syringes inside a nitrogen glovebox. In some cases, 0.3 mL of DPP was added to the TOPSe precursor to enhance nanocrystal yield.[28] In addition, 30 mL of anhydrous octane was loaded into separate syringes. The TOPSe precursor was removed from the nitrogen glovebox and rapidly injected into the reaction vessel. The temperature of the reaction solution was maintained at 130 °C during nanocrystal growth. UV−visible−near-infrared absorption measurements (Cary 5E) were used to monitor nanocrystal growth. Once the desired nanocrystal size was obtained (growth time varied from 20 s to 20 min), the heat source was removed from the reaction vessel and 30 mL of anhydrous octane was swiftly injected into the vessel. (PbSe NC sizes were determined from the optical absorption of the colloidal dispersion using the published calibration curve of Moreels *et al.*[56]) Immediately following the octane injection, the reaction vessel was rapidly cooled to room temperature using an ice bath. To avoid exposing the nanocrystals to atmosphere, the colloidal suspension was cannulated from the reaction vessel into a Schlenk flask (Chemglass) and quickly transferred into the nitrogen glovebox.

All post-synthesis methods necessary to prepare clean NC dispersions were carried out in the nitrogen glovebox. The PbSe NCs were precipitated out of the growth solution using a mixture of anhydrous methanol, butanol, and 200 proof ethanol and isolated *via* centrifuge. After discarding the supernatant, the NCs were washed with anhydrous methanol and redispersed in dry hexane. Precipitation with 200 proof ethanol followed by redispersion in dry hexane was repeated three times. The nanocrystals were then placed in a freezer (−32 °C) for 60 min and filtered through a 0.1 μm PTFE filter to produce a clean dispersion.

Deposition of PbSe NC Films. Initially, colloidal PbSe NCs were deposited as glassy films onto the thin film ZnO by spin-coating the NCs from a 250 mg/mL dispersion in anhydrous octane under nitrogen. Due to the bulky nature of the NC ligands, the spun-cast films were placed in a solution of either 1 M hydrazine or 0.05 M ethanedithiol (EDT) in anhydrous acetonitrile to enhance film conductivity. This technique has been shown to reduce interparticle spacing in similar PbSe NC solids, which has led to remarkable enhancements in particle-to-particle carrier transport within the NC films.[23,28] However, this deposition method frequently produced NC films with hairline cracks that could not be completely filled with subsequent coatings, and approximately 60% of the solar cells assembled with these films resulted in electrical short contacts between the gold and ITO electrodes.

To resolve this issue, we deposited colloidal PbSe NCs onto thin film ZnO using a method based on Klem *et al.*[23] and Luther *et al.*,[28] who deposited PbS and PbSe NCs onto ITO, respectively. Deposition steps were all carried out inside a nitrogen glovebox. For example, to deposit a PbSe NC film where the PbSe NCs are covered with 1,2-ethanedithiol (EDT), the ZnO-coated substrate (thin film ZnO sputtered onto an ITO-patterned glass substrate) was first washed in a solution of 0.05 M EDT in anhydrous acetonitrile by dipping the substrates at a 45° angle into the EDT solution at a rate of 0.5 cm/s. After the residual solvent had evaporated, the ZnO-coated substrates were dipped into a 5 mg/mL dispersion of colloidal PbSe NCs in dry hexane at the same angle and rate. After the hexane had completely evaporated, the substrates were again washed in the EDT solution as previously described. The substrates were then rotated 90°, and the dip-coating process was repeated (first dipped into the PbSe NC colloidal dispersion followed by the EDT wash). After every 4 dips, the backside of the substrate was wiped clean with acetone. (We found that the PbSe NCs did not adhere well to the backside of the glass substrates and would therefore contaminate the EDT solution during the washing process when depositing thick NC films.) The dip-coating process described herein was repeated until the desired thickness was achieved. Under the conditions above, each coating step deposited approximately 10 nm of PbSe NC film. The NC films were not thermally annealed after deposition.

Optical Characterization of Colloidal PbSe NCs and NC Films. Absorption spectra of colloidal PbSe NCs and PbSe NC films were recorded using a Cary 5E UV−vis−NIR spectrophotometer purchased from Varian, Inc. PbSe NC film absorption was measured using transmission through PbSe NC-coated ZnO electrodes (NC film deposited onto ZnO); ZnO electrodes (thin film ZnO sputtered onto ITO-patterned glass substrates) without NCs were used as reference spectra.

Deposition of α-NPD and Gold Contacts. The α-NPD layer and gold contacts were deposited through shadow masks onto photoelectrodes using a custom-built thermal evaporator inside an inert nitrogen glovebox. All depositions were carried out under high vacuum (10^{-6} Torr). α-NPD was deposited between 195 and 205 °C at a rate of ~0.3 Å/s. Immediately following α-NPD deposition, 100 nm thick gold contacts were evaporated onto solar cells at a rate of 0.7 Å/s. The active area of each solar cell was 0.046 cm^2. Assembled solar cells were then placed into nitrogen-purged, sealed receptacles and stored in the glovebox until further characterization.

Solar-Cell Characterization. Solar-cell current−voltage ($I-V$) characteristics were measured using a solar-simulation configuration as in ref 10. Throughout this work, we did not correct for the spectral mismatch between the simulated AM1.5 spectrum and the actual AM1.5G solar spectrum. To maintain the solar cells in an air-free environment during these measurements, the substrates were sealed under nitrogen in a small homemade chamber that allowed optical and electrical access to the solar cells.

Photocurrent action spectra characteristics were recorded using the same solar-cell configuration, but with one slight modification. A second 0.125 m monochromator (Newport, Cornerstone 130) was added to the light source such that the Xe arc lamp now supported two monochromators. While nearly identical to the monochromator used in ref 10, the second monochromator was equipped with a 600 groove/nm grating (blaze wavelength = 750 nm) instead of a 1200 groove/nm grating in order to maximize sensitivity in the near-infrared region of spectral light. In regards to solar-cell characterization, the monochromator used in ref 10 was used to illuminate solar cells with the broad-band AM1.5 spectrum; the second monochromator was utilized to obtain photocurrent action spectra. The slit at the entrance of the second monochromator was adjusted to give a ~20 nm band-pass. A long-wave-pass filter (Newport 59502 or Edmund Industrial Optics RG1000) was placed between the second monochromator and the Xe lamp to eliminate higher-order reflections from the Xe lamp when collecting photocurrent action spectra. The lamp irradiance, $P(\lambda)$, was recorded using a calibrated radiometry system that included a Thermopile sensing probe and a radiant power meter from Newport (70268 and 70260).

Patterning of Gold Back-Gated Si/SiO_2 Field-Effect Transistor Substrates. Si/SiO_2 wafers were patterned using standard liftoff techniques and used as substrates for field-effect transistors (FETs). The wafers were first cleaned by ultrasonication in an equal volume mixture of acetone, IPA, and methanol for 60 min and rinsed with DI water prior to back-side gold deposition and front-side patterning. For back-side gold deposition, thermally grown SiO_2 was first etched from the back-side of the wafers using a buffered oxide etching process. In this process, MICROPOSIT S1818 positive photoresist was spin-coated onto the front-side of wafers at 3000 rpm for 30 s to protect the front of the wafers from the etchant. Residual solvent was driven from the photoresist by baking the wafers at 120 °C for 3 min, and a second layer of S1818 photoresist was cast using the same method. Wafers were then immersed into an etching solution consisting of hydrofluoric acid (9 vol %) in DI water for 8 min (SiO_2 etch rate ≈ 513 Å/min) and thoroughly rinsed with DI water. Thin metallic layers of 10 nm Al/75 nm Au were evaporated onto the back of the wafer using an electron-beam evaporation system (CHA Industries, Model SEC600). The Al/Au depositions were carried out under high vacuum (10^{-6} Torr) at a rate of 1 Å/s for both metals. Following metal deposition, the photoresist was removed from the front side of the wafers by immersing the wafers into a heated acetone bath overnight. To ensure complete removal, the wafers were sonicated in an acetone bath for 30 min. The Au-coated back-gated wafers were cleaned a second time with acetone, IPA, and methanol and blown dry with nitrogen. Finally, the wafers were annealed at 450 °C for 5 min to enhance the quality of the back-side metal contact.

For front-side patterning and contact deposition, wafers were dehydrated for 1 min at 115 °C. To promote adhesion of the photoresist, liquid HMDS was spin-coated onto the wafers' front side at 3000 rpm for 30 s. Next, MICROPOSIT S1818 positive photoresist was spin-coated using the same spin speed and time. To drive off residual solvent from the photoresist, the wafers were baked at 105 °C for 1 min prior to exposure. The photoresist-coated wafers were exposed to UV radiation for 10 s through a chrome mask that defined the source and drain electrodes; multiple source and drain electrodes were patterned to allow for electrical measurements using various channel lengths (5−100 μm). The exposed photoresist was developed by immersing the wafers into a solution of MICROPOSIT MF-351 developer in DI water (50 vol %) for 20 s and then immediately rinsed with excess DI water. Source and drain electrodes consisting of 2.5 nm Cr and 22.5 nm Au were evaporated onto the front of the wafers sequentially at rates of 0.5 and 1.0 Å/s, respectively. Following metal deposition, the excess photoresist on the front side of the wafers was removed by immersing the wafers in a heated acetone bath overnight. To ensure complete removal of the unwanted metal, the wafers were sonicated in an acetone bath for 5 min.

Field-Effect Transistor Characterization and Two-Terminal Conductance Measurements. FET operating and transfer curves and two-terminal $I-V$ characteristics were recorded using a Keithley 236 source-measure unit (source electrode voltage source) and a Keithley 237 high-voltage source-measure unit (drain electrode voltage source) in conjunction with two Keithley 6517 electrometers (gate electrode voltage source). The electrometers were connected to a Desert Cyrogenics vacuum probe station. For all measurements, the source electrode was set to ground ($V_{source} = 0$). Since the vacuum probe station was located outside of an inert glovebox, FET and two-terminal substrates were briefly exposed to atmosphere while in transfer from the glovebox, where they were being stored, to the probe station. To minimize this air exposure, the probe station sample chamber was first purged with nitrogen for 1 min while maintaining a nitrogen pressure slightly greater than atmospheric pressure. During the purge, the substrates to be measured were placed in nitrogen-purged, sealed receptacles while in the glovebox. The capsules were removed from the glovebox and brought to the probe station, where the capsules were opened and the substrates immediately transferred into the sample chamber (<3 s of total air exposure). Measurements were carried out either under vacuum (~10^{-6} Torr) or under 1 atm of nitrogen at room temperature (300 K). A 150 W tungsten halogen light bulb providing 10.5 mW/cm^2 of power was used to illuminate the substrates in the probe station.

Acknowledgment. This work was supported by the NSF under the NIRT program (CTS-0506672). We utilized the University of Minnesota Characterization Facility and the University of Minnesota Nanofabrication Center, which receive partial support from the NSF under the NNIN program. K.S.L. was supported partially by the University of Minnesota Doctoral Dissertation Fellowship during this project. T.J.B. was supported by the REU program of the NSF (DMR-0754792). M.S.K. was supported in part by the MRSEC program of the NSF (DMR-0212302) and by the University of Minnesota Center for Nanostructure Applications. We thank R.J. Holmes, D.M. Stevens, G.H. Lodden, and C.-Y. Liu for valuable discussions and assistance.

Supporting Information Available: Calculation of shunt resistance and field-effect mobilities, XRD spectra, additional solar-cell $I-V$ characteristics, and FET transfer characteristics. This material is available free of charge *via* the Internet at http://pubs.acs.org.

REFERENCES AND NOTES

1. Nozik, A. J. Quantum Dot Solar Cells. *Physica E* **2002**, *14*, 115–120.
2. Kamat, P. V. Quantum Dot Solar Cells. Semiconductor Nanocrystals as Light Harvesters. *J. Phys. Chem. C* **2008**, *112*, 18737–18753.
3. Kongkanand, A.; Tvrdy, K.; Takechi, K.; Kuno, M.; Kamat, P. V. Quantum Dot Solar Cells. Tuning Photoresponse through Size and Shape Control of CdSe−TiO_2 Architecture. *J. Am. Chem. Soc.* **2008**, *130*, 4007–4015.
4. Murray, C. B.; Norris, D. J.; Bawendi, M. G. Synthesis and Characterization of Nearly Monodisperse CdE (E = S, Se,

Te) Semiconductor Nanocrystallites. *J. Am. Chem. Soc.* **1993**, *115*, 8706–8715.
5. Talapin, D. V.; Murray, C. B. PbSe Nanocrystal Solids for n- and p-Channel Thin Film Field-Effect Transistors. *Science* **2005**, *310*, 86–89.
6. Vogel, R.; Pohl, K.; Weller, H. Sensitization of Highly Porous, Polycrystalline TiO_2 Electrodes by Quantum Sized CdS. *Chem. Phys. Lett.* **1990**, *174*, 241–246.
7. Liu, D.; Kamat, P. Photoelectrochemical Behavior of Thin CdSe and Coupled TiO_2/CdSe Semiconductor Films. *J. Phys. Chem.* **1993**, *97*, 10769–10773.
8. Huynh, W. U.; Dittmer, J. J.; Alivisatos, A. P. Hybrid Nanorod−Polymer Solar Cells. *Science* **2002**, *295*, 2425–2427.
9. Gur, I.; Fromer, N. A.; Geier, M. L.; Alivisatos, A. P. Air-Stable All-Inorganic Nanocrystal Solar Cells Processed from Solution. *Science* **2005**, *310*, 462–465.
10. Leschkies, K. S.; Divakar, R.; Basu, J.; Enache-Pommer, E.; Boercker, J. E.; Carter, C. B.; Kortshagen, U. K.; Norris, D. J.; Aydil, E. S. Photosensitization of ZnO Nanowires with CdSe Quantum Dots for Photovoltaic Devices. *Nano Lett.* **2007**, *7*, 1793–1798.
11. Greenham, N. C.; Peng, X. G.; Alivisatos, A. P. Charge Separation and Transport in Conjugated-Polymer/Semiconductor-Nanocrystal Composites Studied by Photoluminescence Quenching and Photoconductivity. *Phys. Rev. B* **1996**, *54*, 17628–17637.
12. Coakley, K. M.; McGehee, M. D. Photovoltaic Cells Made from Conjugated Polymers Infiltrated into Mesoporous Titania. *Appl. Phys. Lett.* **2003**, *83*, 3380–3382.
13. Huynh, W. U.; Dittmer, J. J.; Libby, W. C.; Whiting, G. L.; Alivisatos, A. P. Controlling the Morphology of Nanocrystal−Polymer Composites for Solar Cells. *Adv. Funct. Mater.* **2003**, *13*, 73–79.
14. Coakley, K. M.; Liu, Y. X.; McGehee, M. D.; Frindell, K. L.; Stucky, G. D. Infiltrating Semiconducting Polymers into Self-Assembled Mesoporous Titania Films for Photovoltaic Applications. *Adv. Funct. Mater.* **2003**, *13*, 301–306.
15. Coakley, K. M.; McGehee, M. D. Conjugated Polymer Photovoltaic Cells. *Chem. Mater.* **2004**, *16*, 4533–4542.
16. Vogel, R.; Hoyer, P.; Weller, H. Quantum-Sized PbS, CdS, Ag_2S, Sb_2S_3, and Bi_2S_3 Particles as Sensitizers for Various Nanoporous Wide-Bandgap Semiconductors. *J. Phys. Chem.* **1994**, *98*, 3183–3188.
17. Robel, I.; Subramanian, V.; Kuno, M.; Kamat, P. V. Quantum Dot Solar Cells. Harvesting Light Energy with CdSe Nanocrystals Molecularly Linked to Mesoscopic TiO_2 Films. *J. Am. Chem. Soc.* **2006**, *128*, 2385–2393.
18. Niitsoo, O.; Sarkar, S. K.; Pejoux, C.; Ruhle, S.; Cahen, D.; Hodes, G. Chemical Bath Deposited CdS/CdSe-Sensitized Porous TiO_2 Solar Cells. *J. Photochem. Photobiol. A* **2006**, *181*, 306–313.
19. Lee, H. J.; Yum, J. H.; Leventis, H. C.; Zakeeruddin, S. M.; Haque, S. A.; Chen, P.; Seok, S. I.; Grätzel, M.; Nazeeruddin, M. K. CdSe Quantum Dot-Sensitized Solar Cells Exceeding Efficiency 1% at Full-Sun Intensity. *J. Phys. Chem. C* **2008**, *112*, 11600–11608.
20. Mora-Sero, I.; Gimenez, S.; Moehl, T.; Fabregat-Santiago, F.; Lana-Villareal, T.; Gomez, R.; Bisquert, J. Factors Determining the Photovoltaic Performance of a CdSe Quantum Dot Sensitized Solar Cell: The Role of the Linker Molecule and of the Counter Electrode. *Nanotechnology* **2008**, *19*, 424007.
21. Zaban, A.; Micic, O. I.; Gregg, B. A.; Nozik, A. J. Photosensitization of Nanoporous TiO_2 Electrodes with InP Quantum Dots. *Langmuir* **1998**, *14*, 3153–3156.
22. Yu, P.; Zhu, K.; Norman, A. G.; Ferrere, S.; Frank, A. J.; Nozik, A. J. Nanocrystalline TiO_2 Solar Cells Sensitized with InAs Quantum Qots. *J. Phys. Chem. B* **2006**, *110*, 25451–25454.
23. Klem, E. J. D.; MacNeil, D. D.; Cyr, P. W.; Levina, L.; Sargent, E. H. Efficient Solution-Processed Infrared Photovoltaic Cells: Planarized All-Inorganic Bulk Heterojunction Devices *via* Inter-Quantum-Dot Bridging during Growth from Solution. *Appl. Phys. Lett.* **2007**, *90*, 183113.
24. Luther, J. M.; Law, M.; Beard, M. C.; Song, Q.; Reese, M. O.; Ellingson, R. J.; Nozik, A. J. Schottky Solar Cells Based on Colloidal Nanocrystal Films. *Nano Lett.* **2008**, *8*, 3488–3492.
25. Ma, W.; Luther, J. M.; Zheng, H. M.; Wu, Y.; Alivisatos, A. P. Photovoltaic Devices Employing Ternary PbS_xSe_{1-x} Nanocrystals. *Nano Lett.* **2009**, *9*, 1699–1703.
26. Sun, B.; Findikoglu, A. T.; Sykora, M.; Werder, D. J.; Klimov, V. I. Hybrid Photovoltaics Based on Semiconductor Nanocrystals and Amorphous Silicon. *Nano Lett.* **2009**, *9*, 1235–1241.
27. Murphy, J. E.; Beard, M. C.; Nozik, A. J. Time-Resolved Photoconductivity of PbSe Nanocrystal Arrays. *J. Phys. Chem. B* **2006**, *110*, 25455–25461.
28. Luther, J. M.; Law, M.; Song, Q.; Perkins, C. L.; Beard, M. C.; Nozik, A. J. Structural, Optical and Electrical Properties of Self-Assembled Films of PbSe Nanocrystals Treated with 1,2-Ethanedithiol. *ACS Nano* **2008**, *2*, 271–280.
29. Klem, E. J. D.; Shukla, H.; Hinds, S.; MacNeil, D. D.; Levina, L.; Sargent, E. H. Impact of Dithiol Treatment and Air Annealing on the Conductivity, Mobility, and Hole Density in PbS Colloidal Quantum Dot Solids. *Appl. Phys. Lett.* **2008**, *92*, 212105.
30. Matsushima, T.; Adachi, C. Extremely Low Voltage Organic Light-Emitting Diodes with p-Doped Alpha-Sexithiophene Hole Transport and n-Doped Phenyl-dipyrenylphosphine Oxide Electron Transport Layers. *Appl. Phys. Lett.* **2006**, *89*, 253506.
31. Meng, H.; Herron, N. Organic Small Molecule Materials for Organic Light-Emitting Diodes. In *Organic Light-Emitting Materials and Devices*; Li, Z., Meng, H., Eds.; CRC Press: Boca Raton, FL, 2007; p 295.
32. Tang, C. W.; VanSlyke, S. A. Organic Electroluminescent Diodes. *Appl. Phys. Lett.* **1987**, *51*, 913–915.
33. Kushto, G. P.; Kim, W.; Kafafi, Z. H. Flexible Organic Photovoltaics Using Conducting Polymer Electrodes. *Appl. Phys. Lett.* **2005**, *86*, 093502.
34. Sze, S. M. *Physics of Semiconductor Devices*, 2nd ed.; John Wiley & Sons: New York, 1981; p 122.
35. Gregg, B. A. Excitonic Solar Cells. *J. Phys. Chem. B* **2003**, *107*, 4688–4698.
36. Law, M.; Beard, M. C.; Choi, S.; Luther, J. M.; Hanna, M. C.; Nozik, A. J. Determining the Internal Quantum Efficiency of PbSe Nanocrystal Solar Cells with the Aid of an Optical Model. *Nano Lett.* **2008**, *8*, 3904–3910.
37. Prince, M. B. Silicon Solar Energy Converters. *J. Appl. Phys.* **1955**, *26*, 534–540.
38. Zabierowski, P.; Rau, U.; Igalson, M. Classification of Metastabilities in the Electrical Characteristics of ZnO/CdS/$Cu(In,Ga)Se_2$ Solar Cells. *Thin Solid Films* **2001**, *387*, 147–150.
39. Gao, W. Y.; Kahn, A. Controlled p Doping of the Hole-Transport Molecular Material *N*,*N*′-Diphenyl-*N*,*N*′-bis-(1-naphthyl)-1,1′-biphenyl-4,4′-diamine with Tetra-fluorotetracyanoquinodimethane. *J. Appl. Phys.* **2003**, *94*, 359–366.
40. Pfeiffer, M.; Leo, K.; Zhou, X.; Huang, J. S.; Hofmann, M.; Werner, A.; Blochwitz-Nimoth, J. Doped Organic Semiconductors: Physics and Application in Light Emitting Diodes. *Org. Electron.* **2003**, *4*, 89–103.
41. Harrison, S. E. Conductivity and Hall Effect of ZnO at Low Temperatures. *Phys. Rev.* **1954**, *93*, 52–62.
42. Janotti, A.; Van de Walle, C. G. New Insights into the Role of Native Point Defects in ZnO. *J. Cryst. Growth* **2006**, *287*, 58–65.
43. Van de Walle, C. G. Strategies for Controlling the Conductivity of Wide-Band-Gap Semiconductors. *Phys. Status Solidi B* **2002**, *229*, 221–228.
44. Van de Walle, C. G. Computational Studies of Conductivity in Wide-Band-Gap Semiconductors and Oxides. *J. Phys.: Condens. Matter* **2008**, *20*, 064230.
45. Rothwarf, A. The Superposition Principle for Current in Solar Cells. In Proceedings of the 13th IEEE Photovoltaic Specialists Conference, Washington, DC; IEEE: New York, 1978; p 1312.

46. Rothwarf, A. The CdS/Cu_2S Solar Cell: Basic Operation and Anomalous Effects. *Sol. Cells* **1980**, *2*, 115–140.
47. Miller, W. A.; Olsen, L. C. Current Transport in Boeing (Cd,Zn)/$CuInSe_2$ Solar Cells. *IEEE Trans. Electron Devices* **1984**, *31*, 654–661.
48. Potter, R. R.; Sites, J. R. Light-Induced Junction Modification in (Cd, Zn)S/$CuInSe_2$ Solar Cells. *IEEE Trans. Electron Devices* **1984**, *31*, 571–577.
49. Kylner, A. Effect of Impurities in the CdS Buffer Layer on the Performance of the Cu(In,Ga)Se_2 Thin Film Solar Cell. *J. Appl. Phys.* **1999**, *85*, 6858–6865.
50. Friesen, G.; Dunlop, E. D.; Wendt, R. Investigation of CdTe Solar Cells *via* Capacitance and Impedance Measurements. *Thin Solid Films* **2001**, *387*, 239–242.
51. Agostinelli, G.; Bätzner, D. L.; Burgelman, M. A Theoretical Model for the Front Region of Cadmium Telluride Solar Cells. *Thin Solid Films* **2003**, *431*, 407–413.
52. Hamann, T. W.; Martinson, A. B. F.; Elam, J. W.; Pellin, M. J.; Hupp, J. T. Aerogel Templated ZnO Dye-Sensitized Solar Cells. *Adv. Mater.* **2008**, *20*, 1560–1564.
53. Baxter, J. B.; Aydil, E. S. Nanowire-Based Dye-Sensitized Solar Cells. *Appl. Phys. Lett.* **2005**, *86*, 053114.
54. Law, M.; Greene, L. E.; Johnson, J. C.; Saykally, R.; Yang, P. D. Nanowire Dye-Sensitized Solar Cells. *Nat. Mater.* **2005**, *4*, 455–459.
55. Baxter, J. B.; Walker, A. M.; van Ommering, K.; Aydil, E. S. Synthesis and Characterization of ZnO Nanowires and Their Integration into Dye-Sensitized Solar Cells. *Nanotechnology* **2006**, *17*, S304–S312.
56. Moreels, I.; Lambert, K.; De Muynck, D.; Vanhaecke, F.; Poelman, D.; Martins, J. C.; Allan, G.; Hens, Z. Composition and Size-Dependent Extinction Coefficient of Colloidal PbSe Quantum Dots. *Chem. Mater.* **2007**, *19*, 6101–6106.